Dynamic-scaling exponents and the roughening kinetics of gold electrodeposits

L. Vázquez
Instituto de Ciencia de Materiales, Consejo Superior de Investigaciones Científicas, Departamento de Física Aplicada, C-XII, Universidad Autónoma de Madrid, 28049 Madrid, Spain

R. C. Salvarezza
Instituto de Investigaciones Fisicoquímicas Teóricas y Aplicadas, Sucursal 4, Casilla de Correo 16, 1900 La Plata, Argentina

P. Herrasti, P. Ocón, and J. M. Vara
Departamento de Química Física Aplicada C-II, Universidad Autónoma de Madrid, 28049 Madrid, Spain

A. J. Arvia*
Instituto de Investigaciones Fisicoquímicas Teóricas y Aplicadas, Sucursal 4, Casilla de Correo 16, 1900 La Plata, Argentina
(Received 29 November 1994; revised manuscript received 23 January 1995)

The kinetics of gold electrodeposit roughening was studied at the nanometer level by scanning tunneling microscopy (STM) and by using dynamic-scaling theory. Gold electrodeposits were grown at 100 nm s^{-1} from the electroreduction of hydrous gold oxide layers. The following dynamic-scaling exponents were obtained: $\alpha(I)=0.90\pm0.06$ and $\beta(I)=0.31\pm0.08$ for $L_s<L_{sc}$, and $\alpha(II)=0.49\pm0.05$ and $\beta(II)=0.51\pm0.08$ for $L_s>L_{sc}$, where L_s is the scale length, and L_{sc} is a critical length closely related to the average grain size of the electrodeposit measured from STM imaging. Results from dynamic-scaling analysis are consistent with a grain surface smoothing mechanism involving surface diffusion of gold atoms.

INTRODUCTION

Aggregation processes involved in the growth of a solid phase on a foreign flat solid substrate play a key role in the dynamics and stability of interfaces. In general, the phase growth kinetics can be followed by means of the dynamic-scaling theory applied to surface profiles on different time scales.[1] Thus, for a surface profile of length L consisting of N points, the theory predicts that $\xi(L,\langle h\rangle)$, the interface width, and $\langle h\rangle$, the average profile thickness or height, scale as[1]

$$\xi(L,\langle h\rangle)\propto L^{\alpha}f(x)\ , \tag{1}$$

where $\xi(L,\langle h\rangle)$ is defined by

$$\xi(L,\langle h\rangle)=\left[1/N\sum[h(x_i)-\langle h\rangle]^2\right]^{1/2}\ , \tag{2}$$

and $h(x_i)$ is the deposit height measured along the x direction at the point x_i, where $f(x)=\langle h\rangle/L^z$, with $z=\alpha/\beta$, β and α being the dynamic and static growth exponents, respectively. Furthermore, $f(x)$ has the following properties: $f(x)=$const for $x\to\infty$, and $f(x)=x^{\beta}$ for $x\to0$. Equation (1) comprises two limiting situations, namely

$$\xi(\langle h\rangle)\propto\langle h\rangle^{\beta} \tag{3}$$

for $\langle h\rangle\to0$, and

$$\xi(L)\propto L^{\alpha} \tag{4}$$

for $\langle h\rangle\to\infty$.

Nonequilibrium growth conditions can be produced mainly under the influence of local effects such as stochastic noise, site-dependent growth, and surface relaxation. Growth models such as the Eden,[2] ballistic deposition,[3] and restricted solid-on-solid[4] including this type of contribution result in an object with a nonfractal mass and a self-affine fractal surface. These models can be successfully described by the Kardar, Parisi, and Zhang (KPZ) equation[5] for interface motion which leads to $\beta=0.25$ and $\alpha=0.4$ in $3d$ growth, and $\alpha+z=2$ in all dimensions. Otherwise, those models incorporating surface diffusion lead to either $\alpha=1.0$ and $\beta=0.25$ (Ref. 6) or $\alpha=0.66$ and $\beta=0.20$,[7] fulfilling the linear surface diffusion equation prediction $z=4$.

Nonequilibrium growth conditions are also influenced by nonlocal effects such as those resulting from a Laplacian field. The object grown under these conditions involves either a mass and a surface fractal, as is the case of those objects formed by diffusion-limited aggregation and dendritic growth, or a surface fractal as is the case of dense radial patterns.[8] In this case deposition occurs at protrusions because of Mullins-Sekerka instabilities.

Metal electrodeposition under nonequilibrium conditions has been taken as a model system for the development of complex structures under the influence of local and nonlocal effects. For this type of process at low growth rates, growth should be dominated by local effects leading to a deposit with a nonfractal mass and a self-affine fractal surface obeying Eq. (1).[9,10] In contrast, the interface of $2d$ and $3d$ metal electrodeposits is characterized by α and β values which are far from those predicted by the KPZ equation.[9–11] A qualitative interpretation of this discrepancy was given in terms of nonlocal contribu-

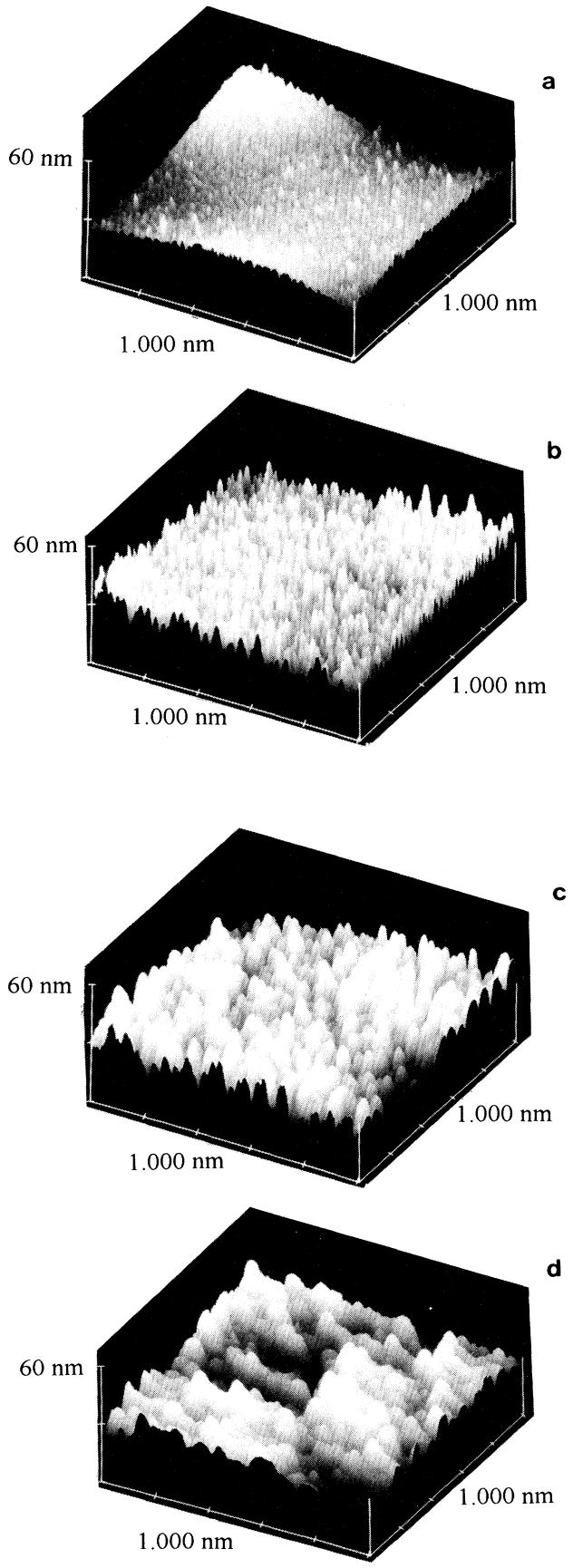

tions to the interface growth,[11] and therefore further work on the matter is clearly justified.

This work reports data on the kinetics of roughening during the formation of gold electrodeposits under non-equilibrium conditions, followed by scanning tunneling microscopy (STM) imaging. For this purpose the dynamic scaling theory is applied to the analysis of STM surface profiles. Data reveal two different surface behaviors with scale-length-dependent roughness exponents. For scale lengths smaller than the average grain size of the deposit ($L < L_{sc}$), the kinetics is definitely dominated by local effects, and the characteristic roughness growth exponents are close to those expected for growth models incorporating surface diffusion. On the other hand, for $L > L_{sc}$, the object growth kinetics appears to be influenced mainly by nonlocal effects.

EXPERIMENT

Gold overlayers were electrodeposited on gold cathodes at a rate $v \cong 100$ nm s^{-1} in 0.5-M aqueous sulphuric acid from the electroreduction of hydrous gold oxide layers previously accumulated in the same solution by gold substrate electro-oxidation at 2.5 V vs the reversible hydrogen electrode (RHE) at $T = 298$ K. Details about gold film preparation procedure have been reported elsewhere.[12] Gold overlayers exhibited a rough surface and a porous mass with a uniform apparent density which was close to that of gold oxide.[12] The value of $\langle h \rangle$, the average gold overlayer thickness, was directly proportional to q, the electrodeposited charge density. The value of q was referred to the geometric substrate area.[12] Accordingly,

$$\langle h \rangle = Mq/zF\rho \ , \tag{5}$$

where M and ρ are the molecular weight and density of the gold oxide overlayer, and zF is the charge per mole of gold oxide. The value of $\langle h \rangle$ was estimated from Eq. (5), using $M = 440$ gr mol^{-1}, $\rho = 11$ gr cm^{-3}, $z = 6$, and measured q values.[12] By changing q the value of $\langle h \rangle$ could be changed between 10 and 12 000 nm.

The surface morphology of gold electrodeposits was determined with a Nanoscope III STM operating in air using the same working conditions already reported.[9] STM data were stored as digitized images with 512×512 pixels, and were analyzed after fitting the instrument plane and applying a subtracting procedure.[9,13]

FIG. 1. Constant current (1000×1000 nm^2) 3d STM images of gold electrodeposits grown at $v \cong 100$ nm s^{-1} on gold at $T = 298$ K. (a) $\langle h \rangle = 35$ nm, (b) $\langle h \rangle = 175$ nm, (c) $\langle h \rangle = 318$ nm, and (d) $\langle h \rangle = 406$ nm. The bar indicates 60 nm in the z direction.

RESULTS AND DISCUSSION

STM images of surfaces of gold overlayers in the range 100 nm $< \langle h \rangle < 12\,000$ nm [Figs. 1(a)–1(d)] reveal the rounded top of columns forming the deposit structure. As $\langle h \rangle$ increases, the surface becomes rougher owing to the stronger competition between growing columns [Fig. 2(a)], leading to a fluctuating growing deposit profile resulting from the columnar height differences. For each value of $\langle h \rangle$, the value of d_s, the average columnar size, was obtained by measuring d, the size of each column tip, from top-view zoom images in which the column tips are

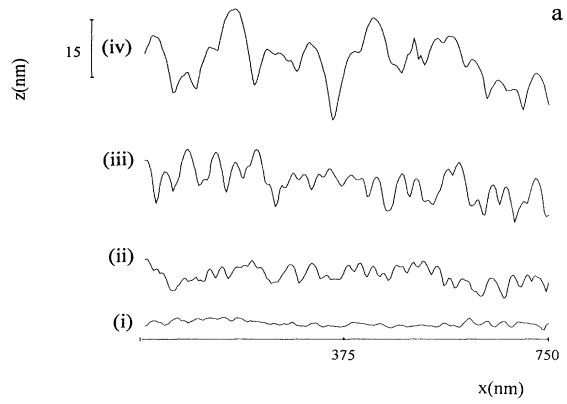

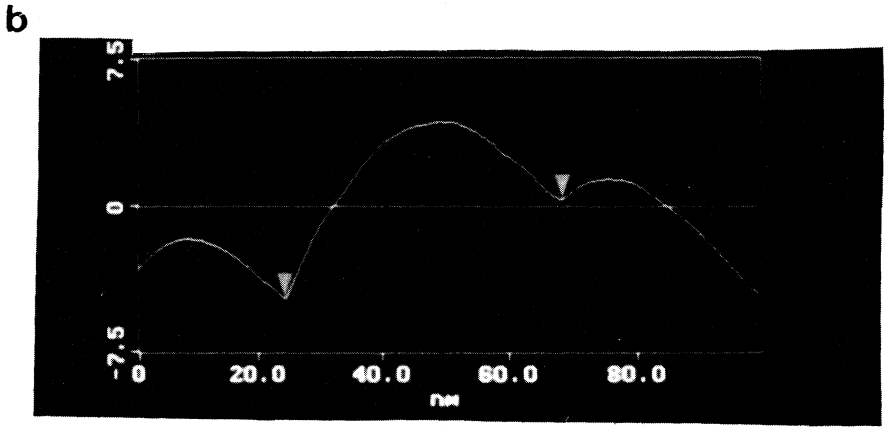

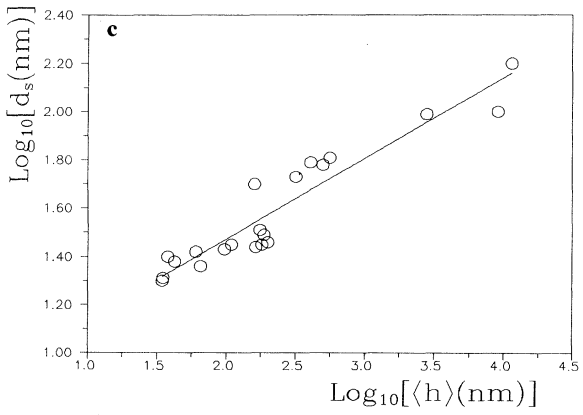

FIG. 2. (a) Typical 750-nm STM scans of gold electrodeposits with different values of $\langle h \rangle$. (*i*) $\langle h \rangle = 20$ nm, (*ii*) $\langle h \rangle = 60$ nm, (*iii*) $\langle h \rangle = 175$ nm, and (*iv*) $\langle h \rangle = 406$ nm. (b) Zoom image cross section illustrating the procedure used for grain size evaluation. (c) $\log_{10} d_s$ vs $\log_{10} \langle h \rangle$ plot.

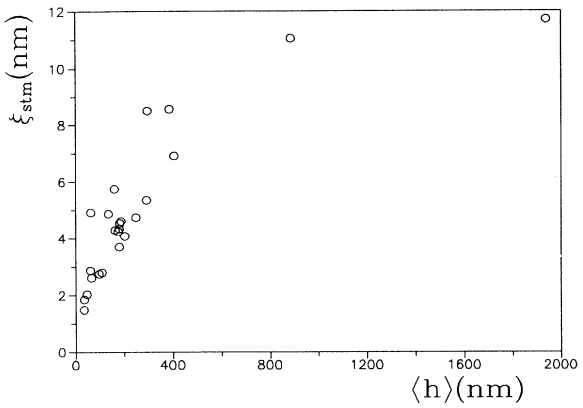

FIG. 3. ξ_{STM} vs $\langle h \rangle$ plot.

clearly defined [Fig. 2(b)]. Accordingly,

$$d_s=(1/N)\sum d \ , \tag{6}$$

where N is the number of columns observed in the STM image. For this purpose the STM software was used. Thus it is found that d_s increases as $d_s \propto \langle h \rangle^{1/z}$ with $1/z=0.34\pm0.06$ [Fig. 2(c)]. The value of $\xi_{STM}(L_s,\langle h \rangle)$, the interface width measured from the STM images in the x direction, increases with $\langle h \rangle$ up to 600 nm, and then it reaches a saturation region for $\langle h \rangle > 800$ nm (Fig. 3).

The single-image dynamic-scaling method[9,14] was used to derive reliable values of α. In this method for a film in the saturation roughness regime, α can be evaluated from the equation

$$\xi_{STM}(L_s,\langle h \rangle) \propto L_s^{\alpha} \ , \tag{7}$$

where L_s is the length of a segment of the STM scan of size S measured in the fast scan direction (x). For each scan 490 pairs of data points (L_s,ξ_{STM}) have been obtained, L_s being varied from $S/128$ to $0.96S$. Finally, for each L_s the corresponding ξ_{STM} value represents the average value resulting from 512 scans of the same image.

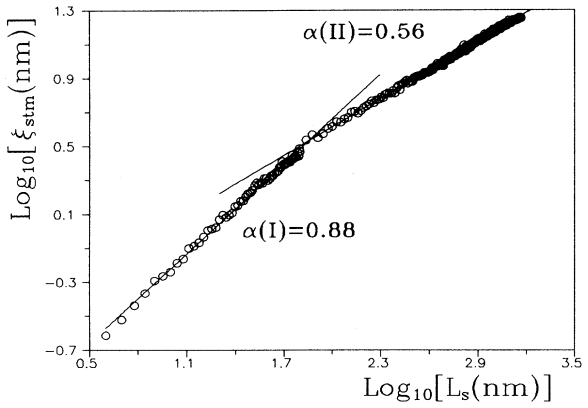

FIG. 4. $\log_{10}\xi_{STM}$ vs $\log_{10}L_s$ plot from gold electrodeposits grown at $v \cong 100$ nm s^{-1} and $T=298$ K. Saturation roughness regime, $\langle h \rangle = 886$ nm.

The $\log_{10}\xi_{STM}$ vs $\log_{10}L_s$ plots from STM images of a gold deposit with $\langle h \rangle = 886$ nm (Fig. 4) exhibit two linear regions with slopes $\alpha(I)=0.88\pm0.02$ and $\alpha(II)=0.56\pm0.02$, and a crossing point at $\log_{10}L_{sc}=1.75$. Although the value of L_{sc} increases as $\langle h \rangle$ increases, $\alpha(I)$ and $\alpha(II)$ values remain nearly constant with $\langle h \rangle$. Values of $\alpha(I)$ and $\alpha(II)$ averaged from 15 different STM images for each value of $\langle h \rangle$, and values of $\langle h \rangle$ in the range 600 nm $< \langle h \rangle <$ 12 000 nm, are $\langle \alpha(I) \rangle = 0.90\pm0.07$ and $\langle \alpha(II) \rangle = 0.49\pm0.07$.

The physical origin of the two regions in the $\log_{10}\xi_{STM}$ vs $\log_{10}L_s$ plots can be assigned to different domains in the columnar structure which are revealed by changing the scale length, i.e., the microscope resolution. The first domain, which is restricted to a scale length in the order of the column size, corresponds to scaling properties at single-column surfaces. The second domain which appears at scale lengths larger than the average columnar size, can be related to column height fluctuations. This interpretation can be supported by scaling computer-simulated surfaces resulting from an ensemble of columns fluctuating in height with known values of α_s [Figs. 5(a)–5(b)]. The surface of each column is represented by a smooth rounded cusp of diameter d_s. For this surface model the $\log_{10}\xi$ vs $\log_{10}L$ plots exhibit one or two linear regions depending on the L/d_s ratio. For $L/d_s \gg 1$ [low resolution limit, Fig. 5(a)] only one region with slope α_s is observed [Fig. 5(c), plot A]. Otherwise, for $L/d_s \leq 20$ [Fig. 5(b)] two linear regions with $\alpha \to 1$ for $L < d_s$, and $\alpha = \alpha_s$ for $L_s > d_s$ are observed [Fig. 5(c), plots B]. In addition, for a given L, the value of L_{sc} increases as d_s is increased [Fig. 5(d), plots B and C]. Finally, for $L/d_s \to 1$ (high resolution limit), only the region with $\alpha \cong 1$ results from the $\log_{10}\xi$ vs $\log_{10}L$ plots. Note that $\alpha \cong 1$ is consistent with a smooth rounded cusp surface.

On the other hand, according to Eq. (3), the value of β can be obtained from $\langle \xi_{STM}(L_s) \rangle$ and $\langle h \rangle$ data for $\langle h \rangle < L_s$. Thus, the $\log_{10}\xi_{STM}$ vs $\log_{10}\langle h \rangle$ plots from 15 STM images for each $\langle h \rangle$ covering the same range of $\langle h \rangle$ mentioned above lead to straight lines (Fig. 6) with L_s-dependent slopes (β). Accordingly, for $\langle h \rangle < L_s$, average values of $\langle \beta \rangle$ converge to $\langle \beta(II) \rangle = 0.51\pm0.08$ (Fig. 7). Unfortunately, no reliable value of $\langle \beta(I) \rangle$ could be derived from these plots, as values of $\langle h \rangle$ are either close to or greater than $d_s \cong L_{sc}$. Nevertheless, this problem can be circumvented by estimating $\langle \beta(I) \rangle$ from the $d_s \propto \langle h \rangle^{1/z}$ relationship,[1,12] as the values of z and $\alpha(I)$ are known. Hence, for $1/z \cong 0.34\pm0.06$ [Fig. 2(a)] and $\langle \alpha(I) \rangle = 0.90\pm0.07$, it results in $\langle \beta(I) \rangle = 0.31\pm0.08$. These values of $\alpha(I)$ and $\beta(I)$ explain why $\beta \to \langle \beta(I) \rangle$ for $\log_{10}L_s \to 1.2$, as the condition $h \ll L^z$ is fulfilled in the entire range of $\langle h \rangle$.

It should be noted that, for computer-simulated fractals, data covering four to five orders of magnitude are required for logarithmic fitting. For experimental systems, however, this goal is less ambitious owing to the existence of inner and outer cutoffs. Then, $\log_{10}\xi_{STM}$ vs $\log_{10}L_s$ linear plots covering at least one order of magnitude or

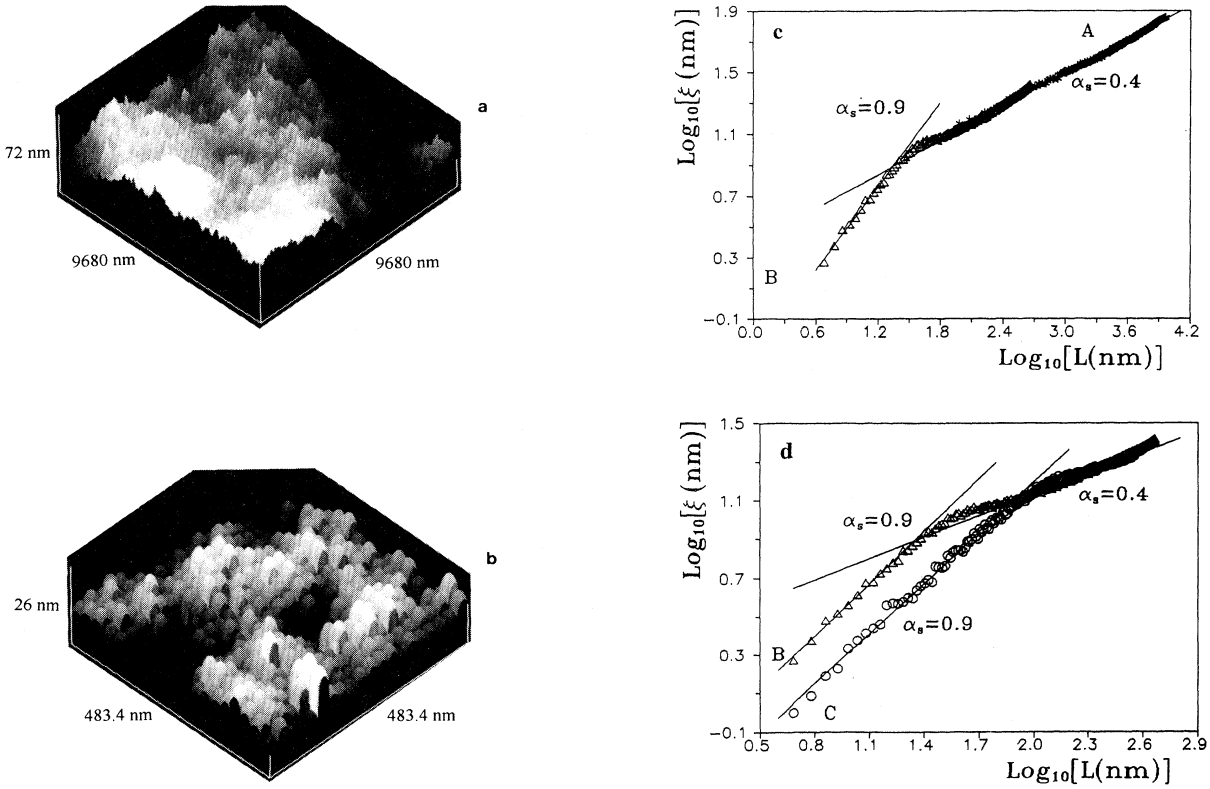

FIG. 5. 3D images of computer-simulated surfaces consisting of fluctuating height columns with $\alpha_s=0.4$ and $d_s=24.2$ nm as described in the text: (a) 9680×9680 nm^2, $L/d_s=400\gg1$; (b) 483.4×483.4 nm^2, $L/d_s=20$; and (c) $\log_{10}\xi$ vs $\log_{10}L$ plots resulting from the scaling of simulated surfaces, with plot *A* (*) : $L=9680$ nm, $d_s=24.2$ nm, and $L/d_s=400$; and plot *B* (△): $L=483.4$ nm, $d_s=24.2$ nm, and $L/d_s=20$. (d) $\log_{10}\xi$ vs $\log_{10}L$ plots resulting from the scaling of simulated surfaces, with plot *B* (△): $L=483.4$ nm, $d_s=24.2$ nm, and $L/d_s=20$; plot *C* (○): $L=483.4$ nm, $d_s=120.9$ nm, and $L/d_s=4$.

thereabouts can be considered as acceptable.[9,13,15]

The dynamic-scaling theory applied to STM data reveals two distinguishable behaviors for the gold overlayer surfaces with specific sets of scale-length-dependent roughness exponents. Thus, for $L<d_s$, $\alpha(I)=0.9$ and $\beta(I)=0.3$, whereas for $L>d_s$ $\alpha(II)=0.5$ and $\beta(II)=0.5$. Similar domain-size-dependent scaling growth exponents have been measured for vapor-deposited gold films grown on smooth glass at $v=0.1$ nm s^{-1} and 298 K.[16] In this case, it resulted in $\alpha(I)=0.9$ and $\beta(I)=0.25$, and $\alpha(II)=0.4$ and $\beta(II)=0.4$ for length scales smaller and larger than the average grain size of the deposit, respectively.

In both cases, for $L_s<d_s$, values of $\alpha(I)$ and $\beta(I)$ are

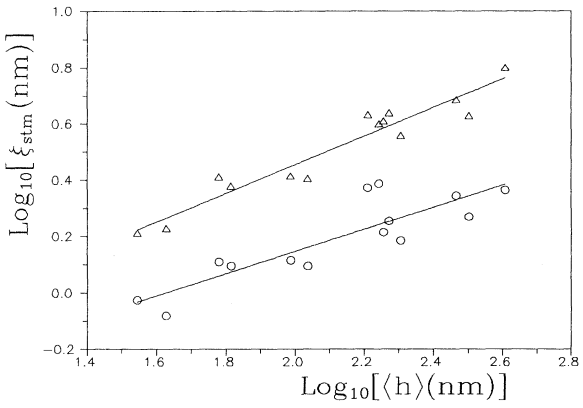

FIG. 6. $\log_{10}\xi_{STM}$ vs $\log_{10}\langle h\rangle$ plots at different values of L_s for gold electrodeposits with $\langle h\rangle<500$ nm, grown at $v=100$ nm s^{-1} and $T=298$ K. (○) $L_s=35$ nm; (△) $L_s=398$ nm.

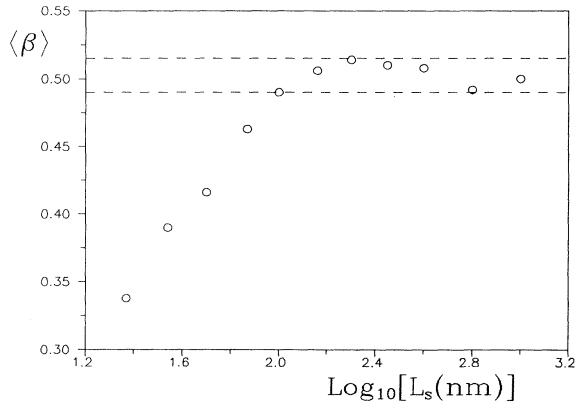

FIG. 7. $\langle\beta\rangle$ vs logL_s plot.

close to those predicted by the growth model incorporating surface diffusion proposed in Ref. 6, suggesting that local effects prevail for $L \leq d_s$. In this case, the condition $z \cong 4$ is fulfilled, as expected for the linear surface diffusion equation.[6,7] Otherwise, for $L > d_s$, $\alpha + z \cong 1.5$, a figure smaller than 2, as is predicted by the KPZ motion equation. In fact, the value $\beta = 0.5$ reported in this work is much greater than $\beta = 0.25$, resulting from the theory and in agreement with experimental data resulting from other systems.[11,17] This difference in the values of β can be accounted for by considering a major contribution of Laplacian fields during gold overlayer electrochemical growth.

In conclusion, based on the analysis of STM images we have demonstrated that there are local and nonlocal effects in the process of roughness development, their relative contributions depending on the yardstick length used for scaling the object.

ACKNOWLEDGMENTS

This work was financially supported by the Consejo Nacional de Investigaciones Científicas y Técnicas of Argentina (CONICET) and Consejo Superior de Investigaciones Científicas of Spain (CSIC) scientific cooperation agreement.

---

*Author to whom all correspondence should be addressed. Fax: 54-21-254642.

[1] F. Family, Physica A **168**, 561 (1990), and references therein.

[2] M. Eden, in *Proceedings of the 4th Berkeley Symposium on Mathematical Statics and Probability,* edited by F. Neyman (University of California Press, Berkeley, 1961), Vol. 4.

[3] P. Meakin, P. Ramanlal, L. M. Sander, and R. C. Ball, Phys. Rev. A **34**, 59 (1986).

[4] G. H. Gilmer and P. Bennema, J. Appl. Phys. **43**, 1347 (1992).

[5] M. Kardar, G. Parisi, and Y. C. Zhang, Phys. Rev. Lett. **56**, 889 (1986).

[6] D. Wolf and J. Villain, Europhys. Lett. **13**, 389 (1990); J. Villain, J. Phys. I **1**, 19 (1992).

[7] Z. W. Lai and S. Das Sarma, Phys. Rev. Lett. **66**, 2348 (1991).

[8] T. Vicsek, *Fractal Growth Phenomena* (World Scientific, Singapore, 1989).

[9] L. Vázquez, R. C. Salvarezza, P. Ocón, P. Herrasti, J. M. Vara, and A. J. Arvia, Phys. Rev. E **49**, 1507 (1994).

[10] G. L. M. K. S. Kahanda, X. Zou, R. Farrell, and P. Wong, Phys. Rev. Lett. **68**, 3741 (1992).

[11] A. Iwamoto, T. Yoshinobu, and H. Iwasaki, Phys. Rev. Lett. **72**, 4025 (1994).

[12] L. Vázquez, A. Bartolomé, A. M. Baró, C. Alonso, R. C. Salvarezza, and A. J. Arvia, Surf. Sci. **215**, 171 (1989), and references therein.

[13] J. Krim, I. Hevaert, C. Haesendock, and Y. Bruynseraede, Phys. Rev. Lett. **70**, 57 (1993).

[14] L. Vázquez, R. C. Salvarezza, P. Herrasti, P. Ocón, J. M. Vara, and A. J. Arvia, *Chaos, Solitons and Fractals,* special volume: *Complex Systems in Computational Physics* (Elsevier, Oxford, in press).

[15] C. Thompson, G. Palasantzas, Y. P. Feng, S. K. Sinha, and J. Krim, Phys. Rev. B **49**, 4902 (1994).

[16] L. Vázquez, R. C. Salvarezza, P. Herrasti, P. Ocón, J. M. Vara, and A. J. Arvia (unpublished).

[17] H. You, R. P. Chiarello, H. K. Kim, and K. G. Vandervoort, Phys. Rev. Lett. **70**, 2900 (1994).

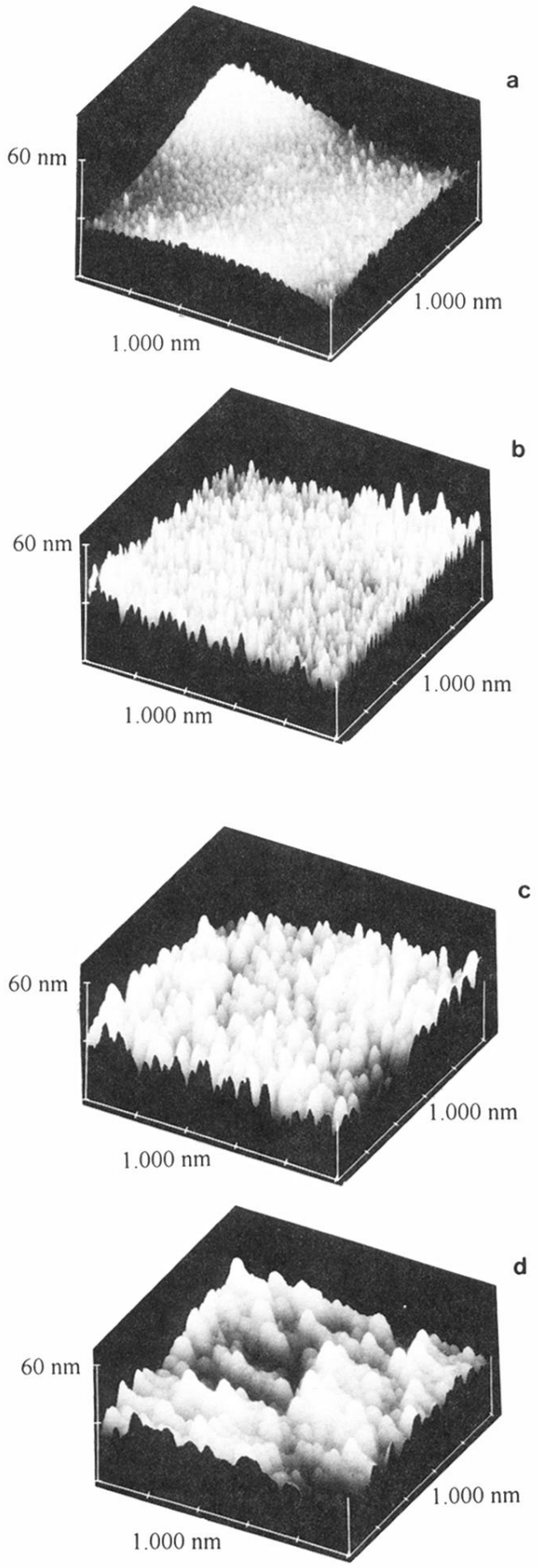

FIG. 1. Constant current (1000×1000 nm^2) $3d$ STM images of gold electrodeposits grown at $v \cong 100$ nm s^{-1} on gold at $T = 298$ K. (a) $\langle h \rangle = 35$ nm, (b) $\langle h \rangle = 175$ nm, (c) $\langle h \rangle = 318$ nm, and (d) $\langle h \rangle = 406$ nm. The bar indicates 60 nm in the z direction.

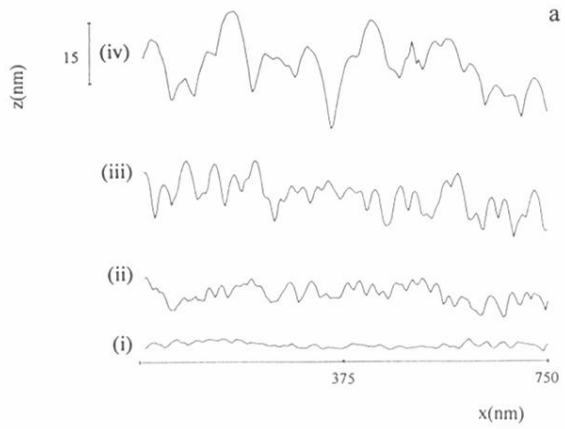

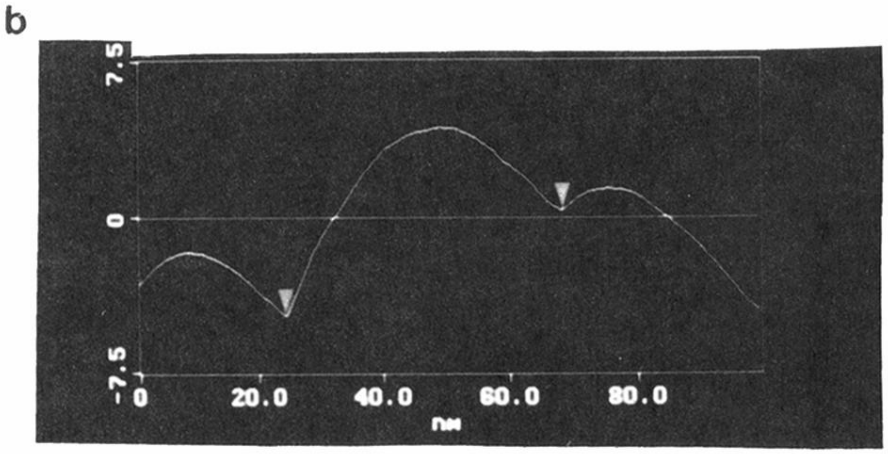

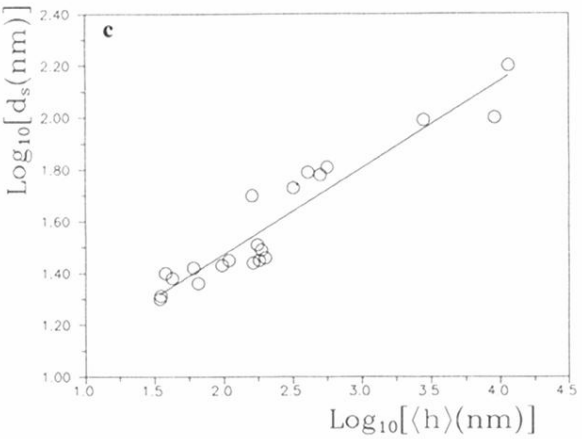

FIG. 2. (a) Typical 750-nm STM scans of gold electrodeposits with different values of $\langle h \rangle$. (*i*) $\langle h \rangle = 20$ nm, (*ii*) $\langle h \rangle = 60$ nm, (*iii*) $\langle h \rangle = 175$ nm, and (*iv*) $\langle h \rangle = 406$ nm. (b) Zoom image cross section illustrating the procedure used for grain size evaluation. (c) $\log_{10} d_s$ vs $\log_{10} \langle h \rangle$ plot.

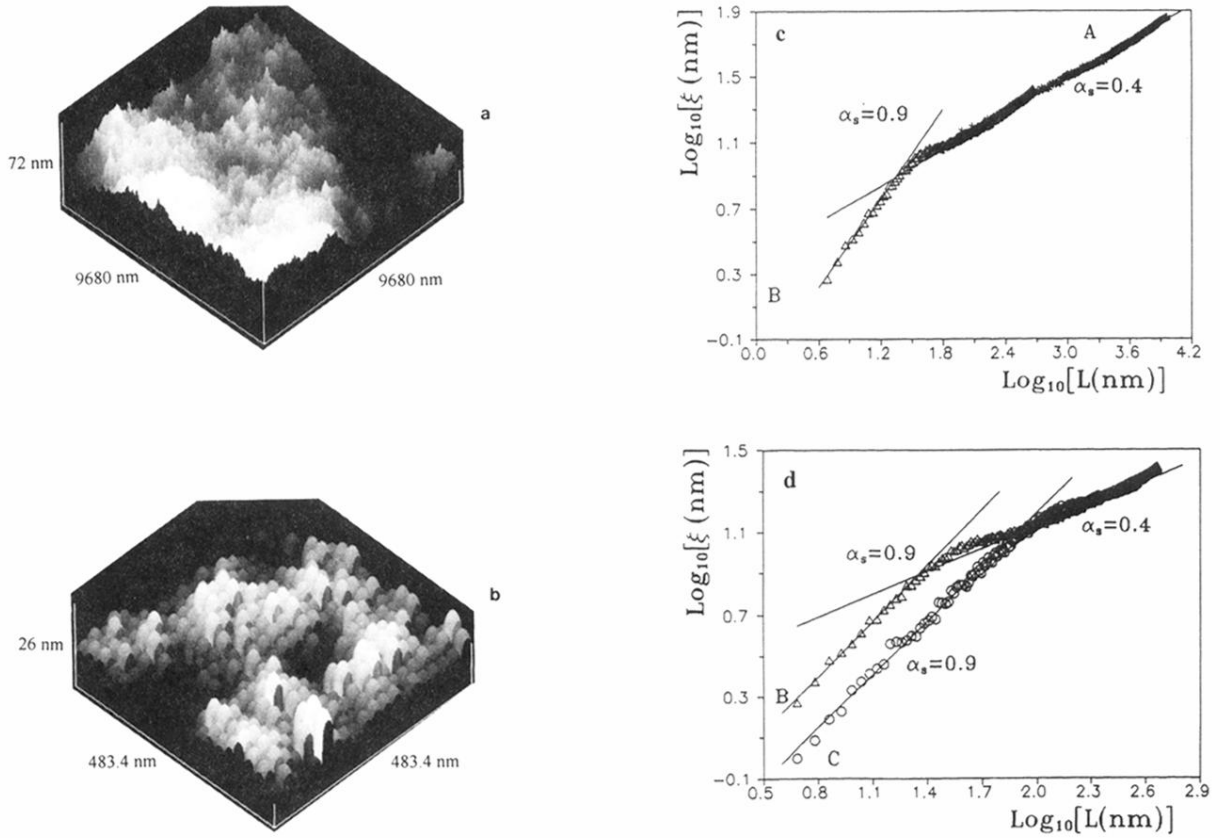

FIG. 5. 3D images of computer-simulated surfaces consisting of fluctuating height columns with $\alpha_s = 0.4$ and $d_s = 24.2$ nm as described in the text: (a) 9680×9680 nm^2, $L/d_s = 400 \gg 1$; (b) 483.4×483.4 nm^2, $L/d_s = 20$; and (c) $\log_{10}\xi$ vs $\log_{10}L$ plots resulting from the scaling of simulated surfaces, with plot A (*) : $L = 9680$ nm, $d_s = 24.2$ nm, and $L/d_s = 400$; and plot B (△): $L = 483.4$ nm, $d_s = 24.2$ nm, and $L/d_s = 20$. (d) $\log_{10}\xi$ vs $\log_{10}L$ plots resulting from the scaling of simulated surfaces, with plot B (△): $L = 483.4$ nm, $d_s = 24.2$ nm, and $L/d_s = 20$; plot C (○): $L = 483.4$ nm, $d_s = 120.9$ nm, and $L/d_s = 4$.